Journal of
Synchrotron Radiation

ISSN 0909-0495

Received 2 November 2012
Accepted 18 January 2013

Heat bump on a monochromator crystal measured with X-ray grating interferometry

Simon Rutishauser,[a]* Alexander Rack,[b] Timm Weitkamp,[c] Yves Kayser,[a] Christian David[a] and Albert T. Macrander[d]

[a]Paul Scherrer Institut, 5232 Villigen PSI, Switzerland, [b]European Synchrotron Radiation Facility, 38043 Grenoble, France, [c]Synchrotron Soleil, 91192 Gif-sur-Yvette, France, and [d]Argonne National Laboratory, Argonne, IL 60439, USA. E-mail: simon.rutishauser@psi.ch

Deformation of the first crystal of an X-ray monochromator under the heat load of a high-power beam, commonly referred to as 'heat bump', is a challenge frequently faced at synchrotron beamlines. Here, quantitative measurements of the deformations of an externally water-cooled silicon (111) double-crystal monochromator tuned to a photon energy of 17.6 keV are reported. These measurements were made using two-dimensional hard X-ray grating interferometry, a technique that enables *in situ* at-wavelength wavefront investigations with high angular sensitivity. The observed crystal deformations were of the order of 100 nm in the meridional and 5 nm in the sagittal direction, which lead to wavefront slope errors of up to 4 µrad in the meridional and a few hundred nanoradians in the sagittal direction.

Keywords: double-crystal monochromator; grating interferometry; wavefront characterization; heat bump.

1. Introduction

Insertion devices at current third-generation synchrotron radiation facilities produce a total radiation power up to the kilowatt range. While a large fraction of this power is cut off by front-end windows, apertures and slits, the remaining radiation power of up to several hundred watts reaches optical elements farther downstream. When using a Bragg monochromator, most of this power is absorbed in the first monochromator crystal and leads to local heating which induces crystal deformations, also referred to as 'heat bump'. The consequences of the deformation are observed as a broadening of the rocking curve, but they also result in an inhomogeneous intensity distribution and deformations of the wavefront. These deformations can be reduced by cooling the first crystal; in many cases silicon monochromators are cooled by liquid nitrogen (Marot *et al.*, 1992; Chumakov *et al.*, 2004), though in some cases water or liquid metal cooling is sufficient.

Here, we investigate a Si-111 double-crystal monochromator that is water-cooled from the sides, measuring the heat bump *in situ*, at-wavelength and under experimental conditions by means of a two-dimensional grating interferometer. Unlike approaches based on crystal shape monitoring using visible-light sensors (Revesz *et al.*, 2007; Thomasset *et al.*, 2010), at-wavelength measurements are easily implemented and measure the effects of the crystal lattice deformations rather than the shape of the crystal surface. A first appreciation of the shape of the first crystal could also be gained from rocking curves, using the second monochromator crystal as an analyzer similar to a diffraction enhanced imaging experiment (Davis *et al.*, 1995; Mocella *et al.*, 2003). However, such an experiment is limited to observing the slope of the first crystal in the meridional direction only; thus such an analysis can only provide an incomplete picture of the heat load effects on the wavefront.

The technique we apply here, hard X-ray grating interferometry, measures the slope of an X-ray wavefront. Since its invention a decade ago (David *et al.*, 2002; Momose *et al.*, 2003), it has become widely used, especially in X-ray imaging of biomedical samples both at synchrotrons (Weitkamp *et al.*, 2005*a*; McDonald *et al.*, 2009; Schulz *et al.*, 2010) as well as at conventional X-ray tube sources (Pfeiffer *et al.*, 2006; Donath *et al.*, 2010; Stampanoni *et al.*, 2011). Recently, grating interferometry has been extended to two dimensions, enabling the simultaneous measurement of the wavefront slope in two perpendicular directions (Zanette *et al.*, 2010; Wen *et al.*, 2010).

Grating interferometry has also found its applications in X-ray metrology at synchrotron sources, measuring the slope errors of mirrors (Weitkamp *et al.*, 2005*b*; Diaz *et al.*, 2010; Wang *et al.*, 2011; David *et al.*, 2012; Matsuyama *et al.*, 2012) or the distortions induced by a single X-ray focusing lens (Rutishauser *et al.*, 2011).

At a free-electron laser source, the technique has been applied to measure the wavefront distortions of single X-ray

pulses and to determine the location of their source point in the undulator (Rutishauser *et al.*, 2012).

The set-up of a two-dimensional grating interferometer is outlined in Fig. 1. It consists of a checkerboard-patterned phase grating G_1 that diffracts the incident radiation mainly into the $\pm$first diffraction orders, both in the horizontal and the vertical direction. These four diffracted waves form a high-contrast interference pattern at specific distances downstream (Primot & Guérineau, 2000; Zanette *et al.*, 2010).

Lateral displacements of this interference pattern are proportional to the wavefront slope. As the interference pattern period is typically smaller than the resolution of the detector downstream, its deformations are detected by introducing an absorbing analyzer grating.

By phase-stepping either the phase grating G_1 or the absorption grating G_2 in multiple steps over one or several grating periods transverse to the beam, a two-dimensional oscillating signal $I(x_g, y_g)$ is recorded at each pixel as a function of the horizontal and vertical grating position x_g and y_g. This signal can be written as a two-dimensional Fourier series (Zanette *et al.*, 2010),

$$I(x_g, y_g) = \sum_{m,n} a_{m,n} \cos\left[(2\pi/p_2)(mx_g + ny_g) + \varphi_{m,n}\right]. \quad (1)$$

Here, $a_{m,n}$ are the Fourier series amplitude coefficients and $\varphi_{m,n}$ their phase. For a phase stepping scan over N grating periods, the phase $\varphi_x = \varphi_{N,0}$ describes the horizontal and $\varphi_y = \varphi_{0,N}$ the vertical distortions of the interference pattern. These distortions are related to the wavefront slope by

$$\alpha_x = \frac{\varphi_x p_2}{2\pi d} - \frac{x}{R_0} + \frac{\Delta\beta y}{d} + \varphi_0, \quad (2)$$

where α_x is the wavefront angle in the horizontal direction, φ_x is the horizontal interference pattern displacement in radians, p_2 is the pitch of the absorption grating and d is the inter-grating distance. Unlike in imaging experiments (Zanette *et al.*, 2010; Rutishauser *et al.*, 2011), no reference measurement without object in the beam can be recorded in the heat bump metrology experiment presented here. As a consequence, additional contributions need to be considered here.

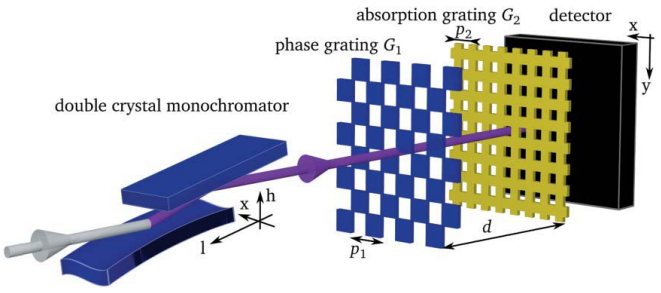

Figure 1
Two-dimensional grating interferometry set-up for measuring the monochromator heat bump. The incident white synchrotron beam is monochromated by the Si-111 double-crystal monochromator. Owing to the high incident power, a heat bump develops on the first monochromator crystal. The grating interferometer measures the wavefront downstream. It consists of a beam-splitting phase grating G_1 of period p_1, which creates an interference pattern that is analyzed by the absorption grating G_2 and a two-dimensional detector.

Grating interferometers are commonly compensated for a certain amount of geometrical magnification between the phase grating and the absorption grating, *i.e.* the phase grating period p_1 is made slightly smaller $p_1 = 2p_2R_0/(R_0 + d)$, such that the interference pattern for a known source distance R_0 and in a specific fractional Talbot distance d has a period that is equal to the absorption grating period p_2. This enables an alignment of the gratings with no residual moiré fringes, and is advantageous in imaging applications. If such a period compensation was implemented, it adds a term x/R_0 to the measured wavefront slope. This term vanishes if the phase grating period is exactly half the absorption grating period and R_0 is infinite.

In addition, any residual rotational misalignment of the two gratings around the optical axis will lead to the emergence of a fraction of a residual moiré fringe. Already a misalignment of a few microradians contributes a non-negligible vertical slope term $\Delta\beta y/d$ to the horizontal wavefront slope α_x. The misalignment between the two gratings, $\Delta\beta$, can be determined quantitatively by means of a grating rotation scan (Wang *et al.*, 2011).

Also, even if gratings and motion control are assumed to be perfect, the measured interference pattern displacements $\varphi_{x,y}$ have an uncertainty in the form of an unknown additive constant φ_0, which is independent of the pixel position (x, y). That is, only variations of $\varphi_{x,y}$ (or, equivalently, $\alpha_{x,y}$) over the field of view are measured, whereas the average angle of wavefront propagation with respect to the interferometer remains undetermined.

From this measurement of the wavefront slope the wavefront phase can be retrieved by a variety of two-dimensional gradient field integration algorithms (Agrawal *et al.*, 2006; Fu *et al.*, 2007).

2. Experimental set-up

The experiments were performed at beamline ID19 at the ESRF (Weitkamp *et al.*, 2010*a*). The Si-111 double-crystal monochromator in Bragg geometry is located at a distance of 140 m from the W150 wiggler source used in this experiment. Its first crystal is 60 mm wide, 160 mm long and 40 mm thick. The monochromator is operated in a helium atmosphere and its first crystal is water-cooled from the sides. The beam footprint on the crystal was 13 mm wide and 110 mm long.

The heat load incident on the monochromator was varied by changing the wiggler gap from 101 mm down to 26 mm. The heat load at the different gap settings was measured by a calorimeter, consisting of a 1.4 kg copper block and a thermocouple that could be moved into the beam directly upstream of the monochromator. The incident power was deduced from the slope of the linear increase of temperature with time in the copper block under white-beam irradiation, and the known heat capacity of copper (Stevens & Boerio-Goates, 2004).

The grating interferometer was placed 10 m downstream of the monochromator, as shown in Fig. 1 and described in detail elsewhere (Weitkamp *et al.*, 2010*b*). The phase grating G_1 was fabricated in silicon by means of a wet etching process (David *et al.*, 2007), with a period of $p_1 = 4.785$ µm and a structure height of $h_1 = 22$ µm providing a π phase shift at the selected photon energy of 17.6 keV. Two line gratings were placed in series, that is, they are effectively the equivalent of a checkerboard-patterned two-dimensional phase grating (Zanette *et al.*, 2010; Rutishauser *et al.*, 2011). At a distance of $d = 448$ mm downstream, corresponding to the 11th fractional Talbot order, a mesh-shaped absorption grating G_2 was installed. It consisted of the superposition of two line absorption gratings of period $p_2 = 2.400$ µm and $h_2 = 60$ µm structure height, which had been fabricated using X-ray lithography and electroplating of gold (Reznikova *et al.*, 2008; Mohr *et al.*, 2012). The rotational misalignment between the horizontal gratings was $\Delta\beta_y = -2.4$ µrad and $\Delta\beta_x = 7.3$ µrad between the vertical gratings, as determined by a grating rotation scan (Wang *et al.*, 2011). The interference pattern was analyzed in a phase stepping scan of 5×5 steps over one grating period, and imaged using a crystal scintillator and a lens-coupled camera (FReLoN 2k type CCD) with 7.5 µm effective pixel size. The camera was mounted such as to observe the central region of the monochromator. The beam size was defined using slits located upstream of the monochromator to only illuminate the region of the monochromator that was within the camera field of view.

3. Heat bump measurements

The horizontal and vertical wavefront slope errors, measured using the two-dimensional grating interferometer, are shown in Fig. 2. The wavefront in the horizontal direction, which is shaped by monochromator slope errors in the sagittal direction, is virtually undistorted; the mean residual wavefront slope error in the horizontal direction is 0.2 µrad (Fig. 2*a*). The corresponding monochromator slope error in the sagittal direction is considerably larger than the resulting wavefront slope error, $\alpha_{x,\mathrm{mono}} = 2\alpha_x/\sin\theta = 17.8\,\alpha_x$, where $\theta = 0.11$ is the Bragg angle of the silicon (111) crystal plane at a photon energy of 17.6 keV. The systematic vertical stripes can be attributed to write field stitching errors of the electron beam writing system used for mask patterning in the grating fabrication process.

Much stronger features can be observed in the vertical wavefront slope error, originating from meridional monochromator slope errors, whose mean residual is 0.9 µrad even at the lowest power level (Fig. 2*b*). Increasing the incident power by closing the wiggler gap leads to increasing distortions and a mean slope error of 1.6 µrad at 12 W and 2.6 µrad at 38 W incident power [Figs. 2(*c*) and 2(*d*)]; clearly a heat bump develops and modifies the vertical wavefront slope. This is also illustrated by the vertical cross sections shown in Fig. 2(*e*) for six wiggler gaps varying from 101 mm in steps of 15 mm down to 26 mm and correspondingly increasing levels of incident power from 8 W to up to 38 W. The horizontal

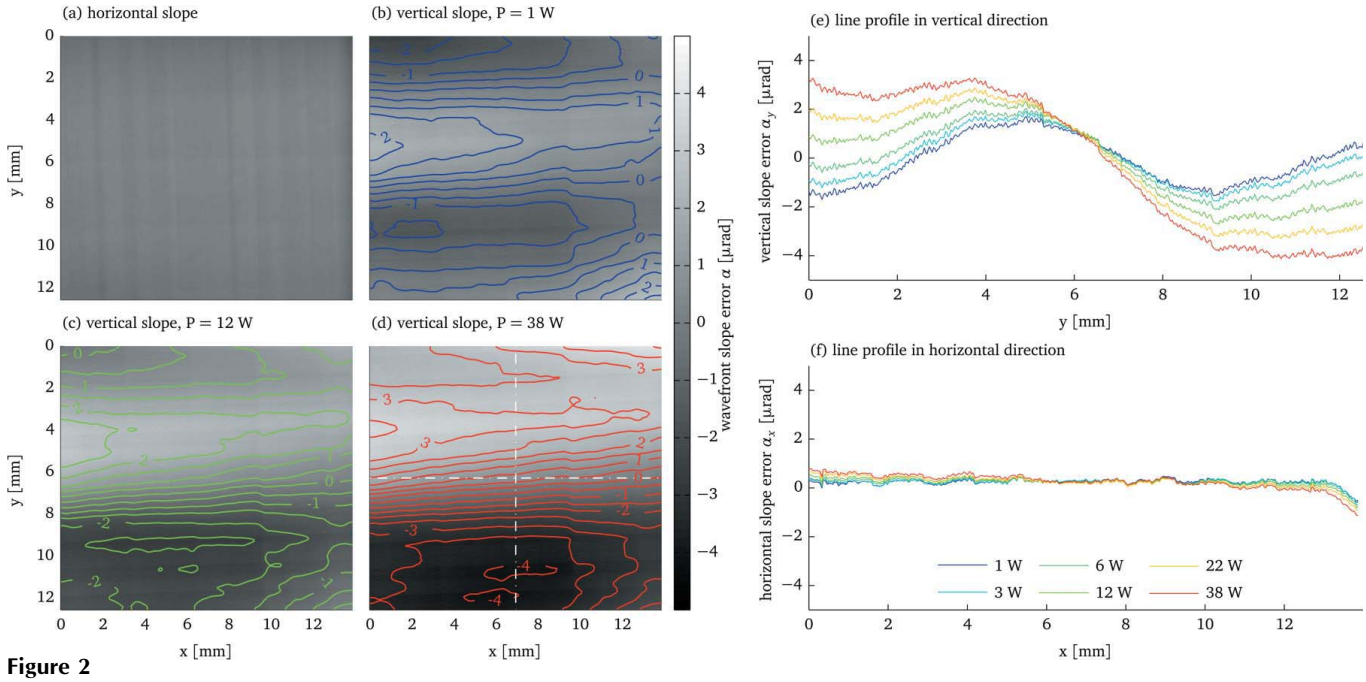

Figure 2
Wavefront slope error measured downstream of the monochromator for increasing incident power. The corresponding slope error of the monochromator in the meridional direction is half of the resulting wavefront slope error, whereas the monochromator slope error in the sagittal direction is considerably larger than the resulting wavefront slope error $\alpha_{x,\mathrm{mono}} = 2\alpha_x/\sin\theta = 17.8\,\alpha_x$, where $\theta = 113$ mrad is the Bragg angle at a photon energy of 17.6 keV. The mean of the plotted data was set to zero, as these are relative measurements; the mean wavefront angle with respect to the interferometer is not measured. (*a*) Horizontal wavefront slope α_x at 1 W incident power. The horizontal slope remains virtually constant independently of the power; it is therefore only shown for the lowest incident power setting. (*b*)–(*d*) Vertical wavefront slope α_y at 1 W, 12 W and 38 W incident power. (*e*, *f*) Line profiles in the vertical and horizontal direction for six different power levels at the location of the dashed lines in (*d*).

wavefront slope error remains stable independently of the incident power, as illustrated by the horizontal cross sections (Fig. 2*f*).

We note that the deduced slope profile corresponds not only to changes in the slope of the surface but also to changes in the Bragg angle due to strain. These two are, in general, combined (Bonse, 1958; Macrander *et al.*, 2005). The separation of these two contributions will rely on finite-element-analyses and diffraction simulations (Mocella *et al.*, 2003) which are planned.

The fine structure on the plotted cross sections, corresponding to slope errors of the order of 100 nrad, is most likely due to grating inhomogeneities, as the gratings used here were not optimized for metrology but rather for imaging of biological samples, where a large gold structure height is more important than the total absence of shape errors. This could be improved by using grating fabrication techniques adapted to the stringent requirements of metrology applications (Rutishauser *et al.*, 2013). However, while the quality of the present gratings does not allow any conclusions as to the surface quality of the monochromator, it is more than sufficient to observe the systematic deformations due to the heat load.

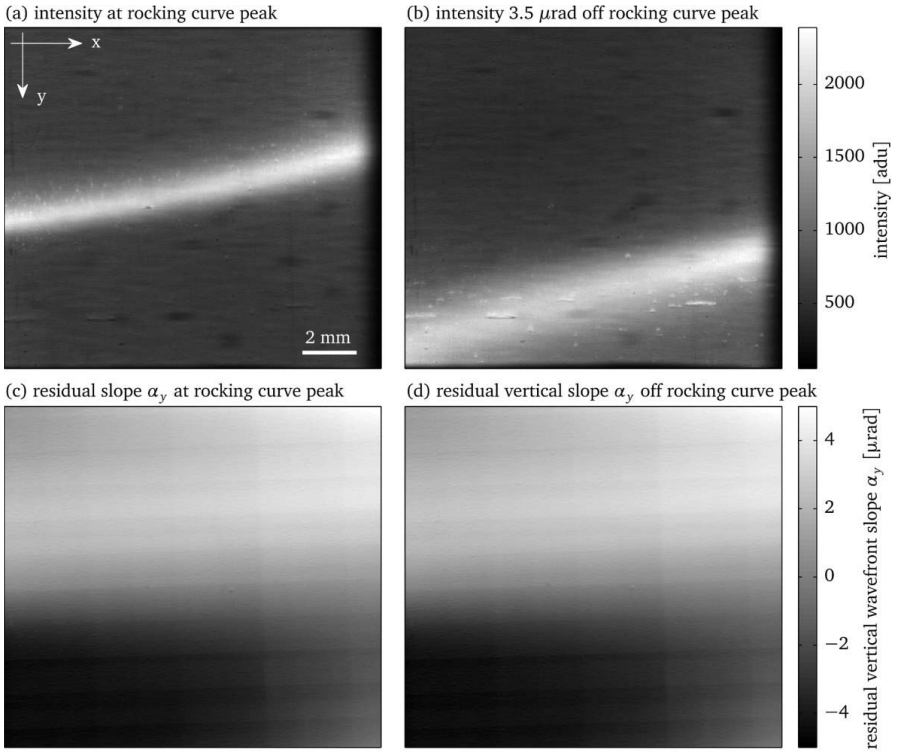

Figure 3
Intensity distribution observed downstream of the monochromator at 38 W incident power. (*a*) Intensity at the rocking-curve peak. (*b*) Intensity at 3.5 μrad off the rocking-curve peak. (*c*) Residual vertical beam angle α_y at the rocking-curve peak. The average angle in the plot was set to zero, as the interferometer only provides relative measurements. (*d*) Residual vertical beam angle α_y at 3.5 μrad off the rocking-curve peak. Relative to the wavefront shown in (*c*), a wavefront slope change of 7 μrad is measured due to the changed monochromator angle; this contribution has been subtracted from the plotted data. After subtraction the relative difference between (*c*) and (*d*) is about 2%.

All the wavefront slope errors plotted here are differences from the slope of a wavefront with a horizontal wavefront radius of curvature of R_x = 160 m and a vertical radius of curvature of R_y = 141 m. These radii were obtained by least-squares fitting a plane to the measurement data obtained at the minimal incident power of 1 W [Figs. 2(*a*) and 2(*b*)]. The actual distance to the wiggler source is R = 150 m (Weitkamp *et al.*, 2010*a*); the difference from the observed radii could be explained by a slight curvature of the monochromator crystals both in the meridional as well as in the sagittal direction even in a thermally unloaded state. This is most likely due to mechanical stress induced by the crystal mounting. The systematic error of these measurements due to errors in the grating period or angular misalignment between phase and absorption gratings is estimated to be less than 5 m.

The heat bump at high levels of incident power has direct consequences, for example in imaging methods such as absorption- or phase-contrast imaging that depend on a clean and stable wavefront. One consequence of the heat bump is that a strong horizontal stripe develops in the beam intensity distribution (Fig. 3*a*). The vertical size of the intensity distribution is about 11 mm independently of the heat load, the observation of a much narrower strip of high intensity indicates diffraction from a heat bump. The stripe is most likely higher harmonic radiation diffracted from the Si-333 crystal plane. Its inclination suggests that one of the monochromator crystals is slightly rotated around the beam axis. While such an inhomogeneity can in principle be compensated for by recording a flat-field image, this makes the imaging process extremely sensitive to drift in the crystal angle and shape; such drift occurs naturally due to the slowly varying heat load on the monochromator over one refill cycle of the storage ring. This effect is illustrated by Fig. 3(*b*), where the second monochromator crystal had been slightly rotated by 3.5 μrad off the rocking-curve peak, which leads to a mean relative change of the intensity in the image by $2(I_a - I_b)/(I_a + I_b)$ = 63%. The corresponding vertical beam angle change recorded by the grating interferometer is 7 μrad, which is twice the angle change of the monochromator. Owing to the high sensitivity of the interferometer configuration used in this experiment, the interference pattern shifts by one entire period for a beam angle change of $\Delta\alpha_{\max}$ = 5.35 μrad. In consequence, this slope change is only measured up to an integer multiple of $\Delta\alpha_{\max}$. However, the component of the signal that is typically used in X-ray phase contrast imaging, which is the residual wavefront angle after subtraction of the average [Figs. 3(*c*) and 3(*d*)], is much less sensitive to such drift

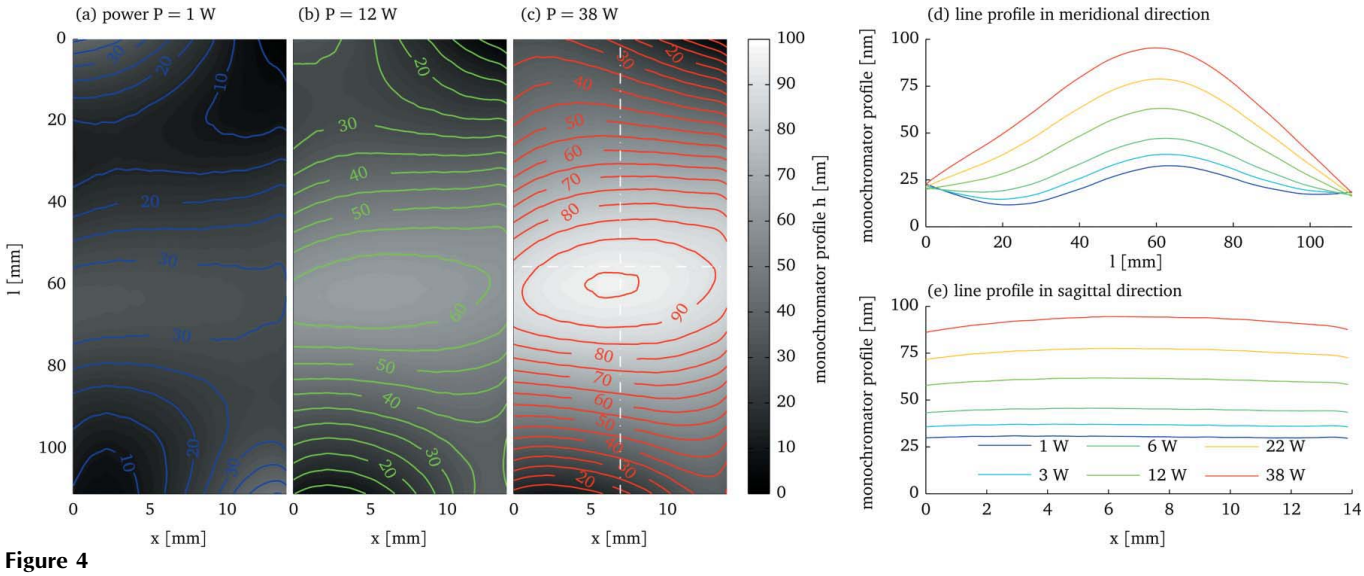

Figure 4
Monochromator profiles obtained from the wavefront profiles for increasing incident power. (*a*)–(*c*) Monochromator surface profile at 1 W, 12 W and 38 W incident power. (*d*)–(*e*) Line profiles of the monochromator profile in the meridional and sagittal direction for six different power levels at the location of the dashed lines in (*c*).

effects. Its mean difference is only 63 nrad, which corresponds to a relative change of only 2%.

Based on the simultaneous wavefront slope measurements in the horizontal and vertical direction (Fig. 2), the integrated wavefront phase Φ was obtained by means of a least-squares optimal gradient field integration algorithm based on a Poisson solver (Agrawal *et al.*, 2006). The wavefront phase Φ is related to the monochromator height profile by $h = \Phi\lambda/(4\pi \tan\theta)$, where $\lambda = 0.7$ Å is the wavelength and $\theta = 113$ mrad is the beam incidence angle on the monochromator. Propagation effects can be neglected, as the interferometer is close to the monochromator, and the spatial frequencies of interest are large.

The resulting monochromator profiles are shown in Fig. 4, where the same spherical contribution and monochromator tilt angle as for the slope data have been subtracted. The residual error at an incident power of 1 W is 20 nm [peak-to-peak, Fig. 4(*a*)]. With increasing heat load it increases to up to 85 nm at 38 W incident power. The monochromator is mainly curved along the meridional direction (Fig. 4*d*), whereas with increasing power its shape only changes by about 5 nm in the sagittal direction. This can mainly be attributed to the much smaller dimensions of the beam footprint in the sagittal direction. The deformations in the meridional direction are quite considerable and are by far the dominant contribution to the monochromator shape error and to the resulting wavefront distortions.

4. Conclusions

Using two-dimensional grating interferometry, we have observed the deformations of the first crystal of a Si-111 double-crystal monochromator *in situ*, at-wavelength and under experimental conditions. Grating interferometry is well suited for measuring the effects of X-ray optical elements on the beam quality, as it is highly sensitive and easy to implement at a synchrotron beamline for a large range of photon energies in the hard X-ray range and beam sizes from several tens of millimeters down to less than a millimeter. The externally water-cooled monochromator under investigation, which is situated at a large distance from the source, was found to be already slightly deformed without heat load, most likely due to stress induced by the mounting. Under the moderate heat loads of less than 50 W applied in this experiment, a considerable heat bump of 85 nm (peak-to-peak) could be observed. However, these deformations are also of a very simple nature and could potentially be countered to a large extent using an active optics design with very few degrees of freedom, such as a simple crystal bending mechanism (Yamaoka *et al.*, 1995).

The authors would like to thank E. Reznikova and J. Mohr, KIT/IMT, for fabrication of the absorption gratings, I. Zanette for discussion and help with preliminary experiments, M. Ruiz Yaniz for help setting up the experiment, A. Khounsary for providing the copper calorimeter, and J. Härtwig for discussion. This work was carried out with the suppport of the Karlsruhe Nano Micro Facility (KNMF), a Helmholtz Research Infrastructure at Karlsruhe Institute of Technology (KIT). TW acknowledges support from RTRA 'Digiteo' and RTRA 'Triangle de la Physique' (grants 2009-034T and 2009-79D). Work performed at Argonne National Laboratory and ATM was supported by the US Department of Energy, Office of Science, Office of Basic Energy Sciences, under contract No. DE-AC02-06CH11357.

References

Agrawal, A., Raskar, R. & Chellappa, R. (2006). *9th European Conference on Computer Vision*, pp. 578–591. Berlin/Heidelberg: Springer.
Bonse, U. (1958). *Zh. Eksp. Teor. Fiz.* **153**, 278.

Chumakov, A., Rüffer, R., Leupold, O., Celse, J.-P., Martel, K., Rossat, M. & Lee, W.-K. (2004). *J. Synchrotron Rad.* **11**, 132–141.
David, C., Bruder, J., Rohbeck, T., Grünzweig, C., Kottler, C., Diaz, A., Bunk, O. & Pfeiffer, F. (2007). *Microelectron. Eng.* **84**, 1172–1177.
David, C., Nöhammer, B., Solak, H. H. & Ziegler, E. (2002). *Appl. Phys. Lett.* **81**, 3287–3289.
David, C., Rutishauser, S., Sprung, M., Zanette, I. & Weitkamp, T. (2012). *AIP Conf. Proc.* **1466**, 23–28.
Davis, T. J., Gureyev, T. E., Gao, D., Stevenson, A. W. & Wilkins, S. W. (1995). *Phys. Rev. Lett.* **74**, 3173–3176.
Diaz, A., Mocuta, C., Stangl, J., Keplinger, M., Weitkamp, T., Pfeiffer, F., David, C., Metzger, T. H. & Bauer, G. (2010). *J. Synchrotron Rad.* **17**, 299–307.
Donath, T., Pfeiffer, F., Bunk, O., Grünzweig, C., Hempel, E., Popescu, S., Vock, P. & David, C. (2010). *Invest. Radiol.* **45**, 445–452.
Fu, Z., Robles-Kelly, A. & Lu, F. (2007). *9th Biennial Conference of the Australian Pattern Recognition Society on Digital Image Computing Techniques and Applications*, pp. 189–195.
McDonald, S. A., Marone, F., Hintermüller, C., Mikuljan, G., David, C., Pfeiffer, F. & Stampanoni, M. (2009). *J. Synchrotron Rad.* **16**, 562–572.
Macrander, A., Krasnicki, S., Zhong, Y., Maj, J. & Chu, Y. (2005). *Appl. Phys. Lett.* **87**, 194113.
Marot, G., Rossat, M., Freund, A., Joksch, S., Kawata, H., Zhang, L., Ziegler, E., Berman, L., Chapman, D., Hastings, J. B. & Iarocci, M. (1992). *Rev. Sci. Instrum.* **63**, 477–480.
Matsuyama, S., Yokoyama, H., Fukui, R., Kohmura, Y., Tamasaku, K., Yabashi, M., Yashiro, W., Momose, A., Ishikawa, T. & Yamauchi, K. (2012). *Opt. Express*, **20**, 24977–24986.
Mocella, V., Lee, W.-K., Tajiri, G., Mills, D., Ferrero, C. & Epelboin, Y. (2003). *J. Appl. Cryst.* **36**, 129–136.
Mohr, J., Grund, T., Kunka, D., Kenntner, J., Leuthold, J., Meiser, J., Schulz, J. & Walter, M. (2012). *AIP Conf. Proc.* **1466**, 41–50.
Momose, A., Kawamoto, S., Koyama, I., Hamaishi, Y., Takai, K. & Suzuki, Y. (2003). *Jpn. J. Appl. Phys.* **42**, L866–L868.
Pfeiffer, F., Weitkamp, T., Bunk, O. & David, C. (2006). *Nat. Phys.* **2**, 258–261.
Primot, J. & Guérineau, N. (2000). *Appl. Opt.* **39**, 5715–5720.
Revesz, P., Kazimirov, A. & Bazarov, I. (2007). *Nucl. Instrum. Methods Phys. Res. A*, **576**, 422–429.
Reznikova, E., Mohr, J., Boerner, M., Nazmov, V. & Jakobs, P.-J. (2008). *Microsyst. Technol.* **14**, 1683–1688.
Rutishauser, S., Bednarzik, M., Zanette, I., Weitkamp, T., Boerner, M., Mohr, J. & David, C. (2013). *Microelectro. Eng.* **101**, 12–16.
Rutishauser, S., Samoylova, L., Krzywinski, J., Bunk, O., Grunert, J., Sinn, H., Cammarata, M., Fritz, D. M. & David, C. (2012). *Nat. Commun.* **3**, 947.
Rutishauser, S., Zanette, I., Weitkamp, T., Donath, T. & David, C. (2011). *Appl. Phys. Lett.* **99**, 221104.
Schulz, G., Weitkamp, T., Zanette, I., Pfeiffer, F., Beckmann, F., David, C., Rutishauser, S., Reznikova, E. & Müller, B. (2010). *J. R. Soc. Interface*, **7**, 1665–1676.
Stampanoni, M., Wang, Z., Thüring, T., David, C., Roessl, E., Trippel, M., Kubik-Huch, R. A., Singer, G., Hohl, M. K. & Hauser, N. (2011). *Invest. Radiol.* **46**, 801–806.
Stevens, R. & Boerio-Goates, J. (2004). *J. Chem. Thermodyn.* **36**, 857–863.
Thomasset, M., Moreno, T., Capitanio, B., Idir, M. & Bucourt, S. (2010). *Nucl. Instrum. Methods Phys. Res. A*, **616**, 197–202.
Wang, H., Sawhney, K., Berujon, S., Ziegler, E., Rutishauser, S. & David, C. (2011). *Opt. Express*, **19**, 16550–16559.
Weitkamp, T., Diaz, A., David, C., Pfeiffer, F., Stampanoni, M., Cloetens, P. & Ziegler, E. (2005*a*). *Opt. Express*, **13**, 6296–6304.
Weitkamp, T., Nöhammer, B., Diaz, A., David, C. & Ziegler, E. (2005*b*). *Appl. Phys. Lett.* **86**, 054101.
Weitkamp, T., Tafforeau, P., Boller, E., Cloetens, P., Valade, J.-P., Bernard, P., Peyrin, F., Ludwig, W., Helfen, L. & Baruchel, J. (2010*a*). *AIP Conf. Proc.* **1221**, 33–38.
Weitkamp, T., Zanette, I., David, C., Baruchel, J., Bernard, P., Bech, M., Deyhle, H., Donath, T., Kenntner, J., Lang, S., Mohr, J., Müller, B., Pfeiffer, F., Reznikova, E., Rutishauser, S., Schulz, G., Tapfer, A. & Valade, J.-P. (2010*b*). *Proc. SPIE*, **7804**, 780406.
Wen, H. H., Bennett, E. E., Kopace, R., Stein, A. F. & Pai, V. (2010). *Opt. Lett.* **35**, 1932–1934.
Yamaoka, H., Freund, A. K., Ohtomo, K. & Krumrey, M. (1995). *Rev. Sci. Instrum.* **66**, 2092–2094.
Zanette, I., Weitkamp, T., Donath, T., Rutishauser, S. & David, C. (2010). *Phys. Rev. Lett.* **105**, 248102.